ChemComm

Silicon Quantum Dot with heavily Boron and Phosphorus Codoped Shell

Journal:	*ChemComm*
Manuscript ID	CC-FEA-02-2018-001612.R1
Article Type:	Feature Article

Journal Name

FEATURE ARTICLE

Silicon Quantum Dot with heavily Boron and Phosphorus Codoped Shell

Minoru Fujii,[a †] Hiroshi Sugimoto[a] and Shinya Kano[a]

Received 00th January 20xx,
Accepted 00th January 20xx

DOI: 10.1039/x0xx00000x

www.rsc.org/

Heavily boron and phosphorus codoped silicon quantum dots (QDs) are dispersible in water without organic ligands and exhibit near infrared luminescence. We summarize the fundamental properties and demonstrate the formation of a varity of nanocomposites.

Introduction

Colloidal solution of silicon (Si) quantum dots (QDs) have been a subject of intensive research due to the superior properties such as the wide wavelength controllability of the luminescence[1-5], the biocompatibility[6-9] and the rich surface chemistry[10, 11]. For the past decade, the quality of colloidal Si QDs has been improved very rapidly. Almost monodispersed Si QDs are developed in a wide size range[1, 5], and the highest photoluminescence (PL) quantum yield (QY) reaches 65% [12]. The most important breakthrough contributing to the QY improvement was the development of the technology to properly functionalize the surface by organic molecules with long alkyne chains[3, 13-17]. The surface molecules passivate surface defects and contribute to the QY improvement. Furthermore, they prevent agglomeration of QDs in nonpolar solvents by steric barriers, and thus very clear colloidal solution is now easily available. Because of the rapid progress of the preparation procedure and the improvement of the quality, research on colloidal Si QDs is shifting to the stage to explore new functions by the formation of a variety of composite nanostructures, which include Si QDs with functional molecules, Si QDs and graphene composites[18], Si QDs and polymer composites[19-25] and Si QDs and plasmonic nanostructure composites[26-28].

Si QDs have intrinsically high affinity for biomedical research due to the biocompatibility and biodegradability. Furthermore, they have luminescence in the near infrared (NIR) transparent window of a biological tissue. A prerequisite property required for the usage in biomedical fields is the hydrophilicity. However, many of organic-functionalized Si QDs developed so far are hydrophobic. Although there have been reports on the development of water-soluble Si QDs[29, 30], the wavelength-controllability and the stability are usually not as good as organic-capped hydrophobic ones. Therefore, development of hydrophilic Si QDs exhibiting highly-efficient, stable, wavelength-controllable luminescence in the NIR range is an important research subject.

Recently, we found that simultaneous doping of boron (B) and phosphorus (P) in Si QDs modifies the physical and chemical properties significantly. The codoped Si QDs have hydrophilic surface and can be dispersed in water and alcohol without any organic functionalization processes. They exhibit size controllable luminescence in the visible to NIR ranges in water. In this article, we focus on the all-inorganic water dispersible Si QDs developed in our group and discuss the fundamental properties and summarize on-going work for the development of new functional materials based on codoped Si QDs. All the data shown in this article are obtained for B and P codoped Si QDs, unless specifically stated.

Preparation of codoped Si QDs

The preparation procedure of codoped Si QDs is summarized in our previous review paper [31]. Briefly, Si, SiO_2, B_2O_3, and P_2O_5 are simultaneously sputtered and a Si-rich borophosphosilicate glass (BPSG) film is deposited on a stainless steel plate. The film is peeled from the plate and annealed in a N_2 gas atmosphere for 30 min to grow codoped Si QDs in a BPSG matrix. BPSG containing codoped Si QDs can also be prepared by simply mixing hydrogen silsesquioxane (HSQ), boric acid and phosphoric acid, and annealing[32]. The most important parameter to determine the size of Si QDs is the annealing temperature. When the temperature is 850 - 1250°C, the size is in the regime where the quantum size effect (QSE) controls the energy level structures (< 10 nm) [2]. When the temperature

[a] Department of Electrical and Electronic Engineering, Graduate School of Engineering, Kobe University, Rokkodai, Nada, Kobe 657-8501, Japan.
† e-mail: fujii@eedept.kobe-u.ac.jp

is 1300 – 1600°C, the size exceeds the QSE regime and the energy band structure becomes practically the same as bulk Si crystal [33]. In this article, we denote these large Si particles as Si nanocrystals (NCs) to distinguish them from Si QDs. Finally, Si QDs or NCs are extracted from a BPSG matrix by hydrofluoric acid (HF) etching and dispersed in methanol. By the same procedure, colloidal solution of Si_xGe_{1-x} alloy QDs can also be produced [34].

Results and discussion

Structural characterization

Transmission electron microscopy. Figure 1(a) shows a picture of a methanol solution, in which Si QDs grown at 1150°C are dispersed [35]. The solution is perfectly clear and light scattering from agglomerates is negligible. The high solution dispersibility is due to the negative surface potential (ζ potential: ~-30mV) [36-39]. Figure 1(b) shows a typical high-resolution transmission electron microscope (TEM) image of a Si QD grown at 1150 °C[37]. For the TEM observation, a methanol solution of Si QDs is dropped on a carbon-coated TEM mesh. The lattice fringes crystallographically equivalent to {111} planes of Si crystal (0.314 nm) are clearly observed. The diameter of the QD is about 5 nm. Detailed TEM studies of codoped Si QDs in a wide size range are performed in Ref. [2].

Figure 1(c) shows a TEM image of Si NCs grown at 1500°C [33]. The NCs are spherical and the diameter is around 100 nm. In the last part of this article, we will show that the large Si NCs are efficient nanoantenna operating in the visible to NIR ranges. Figure 1(d) summarizes the relation between the diameter of Si QDs or NCs and the growth temperature[2, 33]. The diameter is controlled from 1 nm to over 200 nm by changing the growth temperature from 900 to 1600°C. The size also depends on the amount of excess Si in Si-rich BPSG.

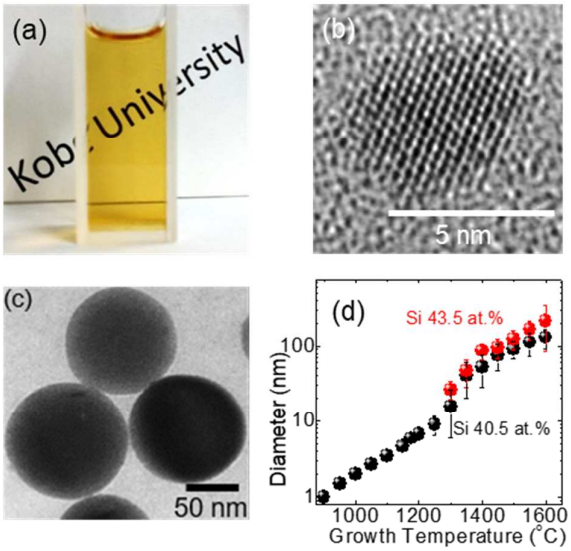

Figure 1 (a) Photograph of a methanol solution of codoped Si QDs. (b) High-resolution TEM image of a Si QD grown at 1150°C. (c) TEM image of Si NCs grown at 1500°C. (d) The relation between the diameter of Si QDs or NCs and the growth temperature. (a) Reproduced from Ref. [35]. Copyright 2013 American Chemical Society. (b) Reproduced from Ref. [37]. Copyright 2012 American Chemical Society. (c) Reproduced from Ref. [33]. Copyright 2017 Wiley-VCH Verlag GmbH & Co.

A characteristic feature of the codoped Si QDs or NCs is the high dispersibility in polar solvents, which arises from the heavily B and P codoped inorganic shell surrounding Si QDs or NCs. The evidence of the formation of the shell is obtained by electron energy loss spectroscopy [37] and Raman spectroscopy [40]. Very recently, we also succeeded in directly visualizing the shell by TEM by using an atomically thin graphene oxide support film [41]. Furthermore, the very high resistance of codoped Si QDs to HF [35] also supports the formation of a shell composed of chemically stable BP clusters and the derivatives. In fact, small modification of the composition of Si-rich BPSG results in the growth of cubic BP NCs [42] and BSiP NCs [43] instead of codoped Si QDs.

Atom probe tomography. Atom probe tomography (APT) is a powerful tool to visualize dopant distribution in a QD with an atomistic resolution [44-48]. The left-most image in Figure 2(a) is a three-dimensional reconstruction of Si distribution in a needle-shaped tip of BPSG in which codoped Si QDs are grown at 1150°C [47]. A 7 nm thick sliced image in the z-direction is also shown below the tip. We can see the growth of Si QDs in BPSG clearly. Comparison of the image with those of B and P reveals that they are enriched at the positions where the local Si density is high, indicating that they are accumulated during the growth of Si QDs. An APT image of an individual codoped Si QD about 4 nm in diameter is shown in Figure 2(b). The image confirms that B and P atoms are successfully incorporated into the Si QD and that majority of B and P are near the surface of the Si QD. Quantitative information on the distribution of B and P is obtained by the proxigram analysis. Figure 2(c) shows the proxigram profiles for Si QDs grown at 1250°C. In Figure 2(c), the distance at 0 nm represents the interface between the Si QD and the matrix, which is defined at the position where the proxigram profiles of Si and O intersect. The positive distance represents the inside of a Si QD, while the negative one represents the BPSG matrix. We can clearly see accumulation of B at the interface region. On the other hand, the peak concentration of P is slightly inside the interface.

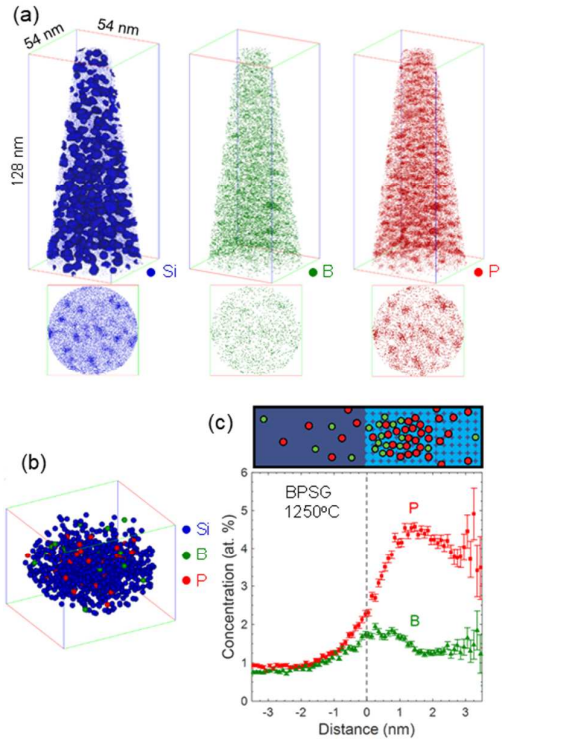

Figure 2 (a) APT of codoped Si QDs in a BPSG matrix grown at 1150°C. (b) APT image of an individual codoped Si QD about 4 nm in diameter. (c) Proxigram profiles for Si QDs grown at 1250°C. Reproduced from Ref. [47]. Copyright 2016 American Chemical Society.

It is noted that the data in Figure 2 are obtained for Si QDs in a BPSG matrix. The interface in Figure 2(c) may be shifted if Si QDs are extracted from BPSG by HF etching. Recently, we have succeeded in performing APT analyses of colloidal Si QDs by re-dispersing them in a dielectric matrix. The preliminary results indicate that the structure is not strongly modified by the HF etching (not yet published).

Electronic states

Photoluminescence. The codoped Si QDs exhibit the size-controllable PL. Figure 3(a) shows PL spectra of methanol solutions of codoped Si QDs grown at different temperatures [2]. The PL peak energy is controlled from 0.9 eV to 1.85 eV. Since the band gap energy of bulk Si crystal is 1.12 eV at room temperature, the controllable range of the PL energy covers both above and below the bulk band gap. The below bulk band gap PL suggests that donor and acceptor states are involved in the optical transition of codoped Si QDs.

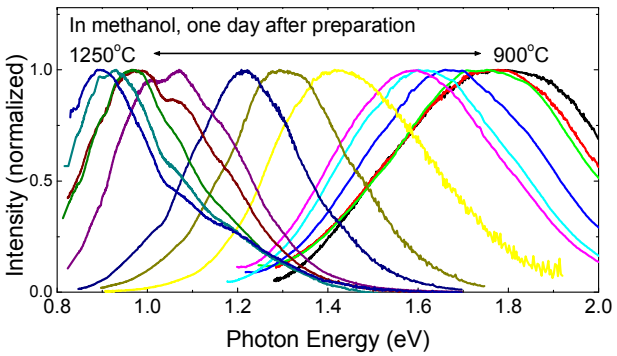

Figure 3 (a) PL spectra of a methanol solution of codoped Si QDs. The growth temperature is changed from 900 to 1250°C. The spectra are measured one day after preparation. Dips around 1 eV are due to absorption by methanol. Reproduced from Ref. [2]. Copyright 2013 American Chemical Society.

The PL spectra of codoped Si QDs are usually broader than those of undoped Si QDs. The full width at half maximum (FWHM) is about 400 meV around 1.6 eV. The broadening is partly due to the size distribution. To lift the size distribution, we measured PL of single codoped Si QDs by micro PL spectroscopy [49]. Figure 4(a) shows the PL spectra of Si QDs on a quartz substrate at room temperature. The spectrum labeled "Ensemble" is obtained from an area containing about 100 Si QDs, while others are the spectra of single Si QDs. The FWHM of the ensemble is 426 meV, which is similar to that of the colloidal solution. The PL of single Si QDs is much narrower than the ensemble PL. This proves that the very broad PL of an ensemble is partly due to the distribution of PL peak energies.

In Figure 4(b), the PL FWHM at room temperature is plotted as a function of the detection energy. The FWHM is distributed from 100 to 350 meV. In the same figure, the FWHM of undoped Si QDs taken from literatures are also shown [50-58]. In undoped Si QDs, the FWHM is in the range 50-200 meV. Therefore, PL of codoped Si QDs is roughly twice as broad as that of undoped ones. The difference between codoped and undoped Si QDs increases at low temperature. The PL FWHM of undoped Si QDs decreases to below 50 meV at 77 K [58-60], while that of codoped Si QDs does not strongly depend on the temperature [49]. The mechanism of the broadening of the PL by B and P codoping is not clear. A possible mechanism is the strong localization of photoexcited carriers around impurity atoms and the distortion of the lattice by the strong electron-phonon coupling. Distribution of the energy of the impurity states due to that of the location also broadens the spectrum. However, the explanation is very primitive. In order to understand the mechanism of the broadening, more precise modeling of the structure and the calculation of the energy structure of the excited state is necessary.

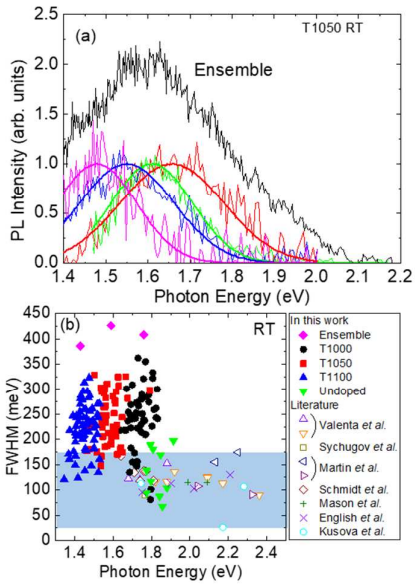

Figure 4 (a) PL spectra of an ensemble of codoped Si QDs and normalized PL spectra of single codoped Si QDs at room temperature. (b) Relation between the PL FWHM and the peak energy. Open symbols represent the data of undoped Si QDs obtained from Refs. [50-58]. Reproduced from Ref. [49]. Copyright 2016 AIP Publishing LLC.

HOMO and LUMO. In codoped Si QDs, donor and acceptor states are considered to be the lowest unoccupied molecular orbital (LUMO) and the highest occupied molecular orbital (HOMO), respectively. Figure 5 shows the size dependence of the HOMO and the LUMO of codoped Si QDs [61]. The ordinate is the energy measured from the vacuum level. The HOMO is obtained from photoemission yield spectroscopy, while the LUMO is determined by adding the PL peak energy to the HOMO level energy. The energy of the Fermi level measured from the HOMO level is obtained by valence band X-ray photoelectron spectroscopy (XPS) spectra. The HOMO level of large Si QDs is above the valence band edge of bulk Si crystal. This confirms that the HOMO level is the acceptor level. Similarly, the LUMO level of large Si QDs is below the conduction band edge of bulk Si crystal and is considered to be the donor level. With decreasing the size, the HOMO level goes down and the LUMO level goes up. The Fermi level of large Si QDs is close to the HOMO level and it approaches to the middle of the band gap with decreasing the size.

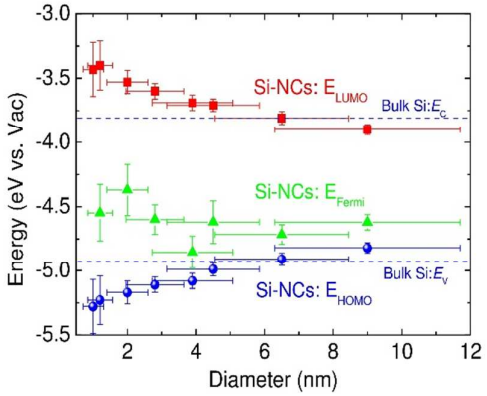

Figure 5 HOMO (•), LUMO (■) and Fermi level (▲) energies measured from the vacuum level of B and P codoped Si-QDs. The horizontal dashed lines are the conduction and valence band edges of bulk Si crystal. Reproduced from Ref. [61]. Copyright 2016 American Chemical Society.

The data in Figure 5 is obtained for ensembles of large number of Si QDs and thus reflect a variety of inhomogeneity, such as the size, shape, B and P concentration, etc. To avoid them, we measure the density of state spectrum of a single codoped Si QD by scanning tunnelling spectroscopy (STS) [62], which was previously used for the analysis of the energy level structure of undoped Si QDs [63-65]. Figure 6(a) is a scanning tunnelling microscope (STM) topographic image of a monolayer of codoped Si QDs placed on an atomically flat Au (111) substrate. Figure 6(b) is a topography cross-section taken along the line in (a). Si QDs are clearly recognized in the image. Figure 6(c) shows a representative *dI/dV* (derivative conductance)-*V* (applied voltage) tunnelling spectrum, which is proportional to the density of the electronic state, acquired from the 7 nm Si QD shown in (a) by a double barrier tunnel junction configuration shown in the inset. The Fermi level resides at V=0. Two small peaks are seen around -0.5 V and 0.7 V, and the outside of the peaks, sharp rises appear at both negative and positive biases. The most plausible explanation of the structure is that the peaks correspond to acceptor and donor levels formed in the band gap by codoping, while the sharp onsets of the density of states correspond to the valence band and conduction band edges. It should be stressed here that the peaks are observed only for codoped Si QDs and all undoped Si QDs we studied are free of any in-gap states [62].

The energy difference between the two peaks depend strongly on the size of Si QDs. In Figure 6(d), the acceptor-donor energy separation obtained from the STS data is plotted as a function of a Si QDs diameter. We can see clear size dependence in the energy separation. The energy separation agrees very well with the PL energy. This confirms that the low energy shift of the PL by B and P codoping is due to the formation of donor and acceptor states in the band gap.

In Figure 6(e), the band gap defined by the energy separation between the valence band edge and the conduction band edge determined by STS is plotted as a function of the size. The asterisk is a datum obtained for undoped Si QDs prepared by the same procedure as codoped Si QDs by using pure silica as a matrix. The data of undoped Si QDs prepared by different procedures [63] is also shown. As expected from the QSE, the band gap increases with decreasing the size. The band gap of codoped and undoped Si QDs are very similar. This suggests that doping does not strongly modify the energy level structures of host Si QDs in the size range and simply introduces donor and acceptor states in the band gap.

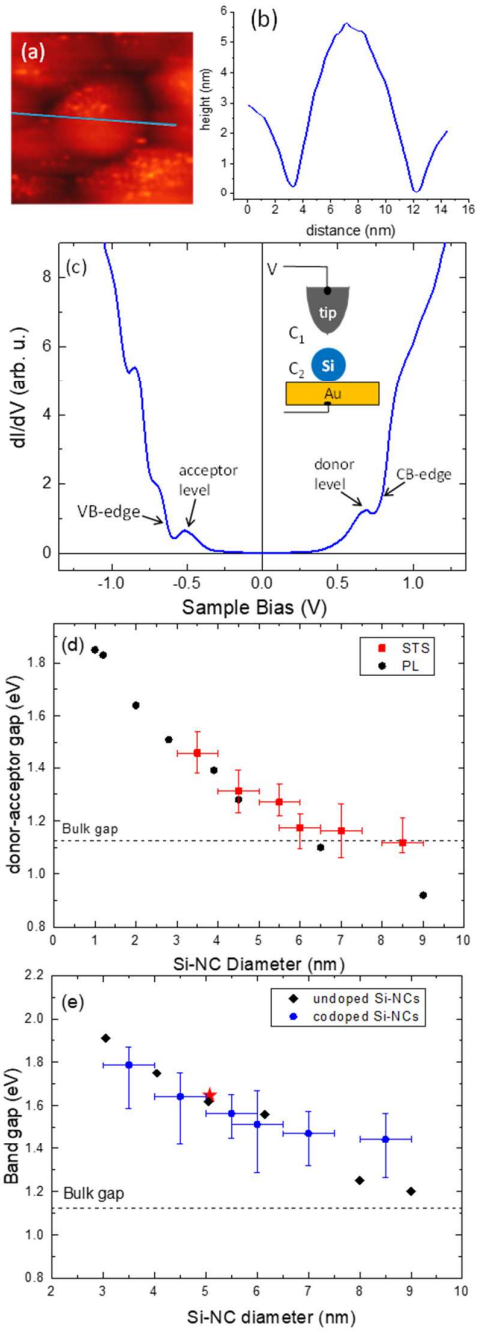

Figure 6 (a-c) STM and STS measurements of a codoped Si QD 7 nm in diameter. (a) STM image, (b) height cross-section taken along the line in (a), and (c) dI/dV-V characteristics taken in a double barrier tunnel junction configuration in the inset. (d) Donor–acceptor gap measured by STS (red squares) and PL peak positions taken from Ref. [2] (black circles) as a function of Si QD diameter. (e) Band gap (black diamond) of codoped Si QDs extracted from the STS data as a function of diameter. The data for undoped Si QDs prepared by the same group (red asterisk) and by a different group (black diamonds) [63] are also shown. Reproduced from Ref. [62] with permission from The Royal Society of Chemistry.

The data in Figure 5 and 6 can be directly compared with theoretical calculations. Detailed comparison between the experimental and theoretical data is very important for better understanding of the energy level structures of codoped Si QDs and for the prediction of the electrical and optical properties. Theoretical studies of impurity-doped Si QDs have been conducted for several decades by many groups. For example, the group of Ossicini studied the energy level structure of codoped Si QDs in detail by ab-initio calculations. Their achievements is summarized in their latest review paper [66]. Exploration of more rigorous theoretical approaches have been performed recently [67]. The most important result obtained in these theoretical work is that the formation energy of Si QDs is drastically reduced by doping exactly the same number of B and P simultaneously. This suggests that perfectly compensated Si QDs, *i.e.*, Si QDs containing exactly the same number of B and P, are preferentially grown if we grow doped Si QDs from Si-rich BPSG. Another important result is that B and P are doped preferentially as a pair, *i.e.*, they are the nearest neighbour each other. Furthermore, the B-P pairs stay preferentially near the surface of a Si QDs with B more outer surface than P. These theoretical predictions are qualitatively in good agreement with our experimental results. However, the size of Si QDs being subjected to ab-initio calculations is usually smaller than 2 nm. Therefore, the overlap of the size range between experiments and calculations are very small, which is a serious obstacle for deep understanding of the structure and the electronic states of codoped Si QDs.

Charge transfer and energy transfer

Photocatalytic activity. We now turn our attention to the interaction between Si QDs and molecules on the surface. In 2002, Kovalev et al. found that Si QDs excite adsorbed oxygen molecules (O_2) to the singlet state, *i.e.*, singlet oxygen generation [68-73]. Singlet oxygen is a kind of active oxygen species [74-76] and mediates important processes in chemistry and biology, such as a photodynamic cancer therapy [77]. The mechanism of the energy transfer from Si QDs to O_2 is the Dexter energy transfer process[78]. More specifically, it is the triplet-triplet annihilation process, which exchanges electrons between a triplet exciton in a Si QD and a triplet ground state of a O_2 molecule[69, 72].

The observation of photosensitized singlet oxygen generation by Si QDs suggests that they can be a photocatalyst for other materials. A prerequisite condition for efficient charge transfer between Si QDs and molecules is a narrow tunnelling barrier between them. Although hydrogen (H)-terminated Si QDs may have the narrowest tunnelling barrier, surface H atoms are usually not very stable in oxygen (O)-rich environment. Furthermore, H-terminated Si QDs are hydrophobic, which is an obstacle for the biomedical applications. Although organic functionalized Si QDs are stable in solution, the organic ligands act as a tunnelling barrier for charge transfer.

The high water dispersibility of codoped Si QDs without organic capping is a great advantage for the usage as a photocatalyst in aqueous environment. In order to demonstrate the potential of codoped Si QDs as a photocatalyst, we study photocatalytic bleaching of a dye molecule in water [79]. We chose Rhodamine B (RhB) as a test molecule. As shown in Figure 7(a), the LUMO level of RhB (-3.88 eV) [80] is slightly higher than that of Si QDs 9 nm in diameter, and thus efficient electron transfer from

photoexcited Si QDs to RhB is not expected. On the other hand, in smaller Si QDs, electron transfer from the LUMO of Si QDs to that of RhB is expected due to the high energy shift of the Si QDs LUMO by the QSE. Figure 7(b) shows the results of the photo-bleaching experiments for Si QDs 4.5 nm in diameter. By light irradiation, the absorption by RhB around 556 nm decreases. On the other hand, in Si QDs 9.0 nm in diameter (Figure 7(c)), the bleaching is less prominent. Figure 7(d) shows normalized absorbance of RhB (at 556 nm) as a function of irradiation time for different size Si QDs. Clear size dependence is seen in the bleaching rate. In Ref. [79], the size dependence of the rate is discussed quantitatively. Furthermore, the size dependence of the charge transfer rate is obtained from the analysis of the PL decay curves of Si QDs. It is shown that the logarithm of the reaction rate and the charge transfer rate is proportional to the energy difference between the LUMOs of Si QDs and RhB[79].

The data in Figure 7(b)-(d) are obtained for Si QDs stored 10 days in methanol, while those in Figure 7(e) are obtained for Si QDs stored 30 days in methanol. Even after 30 day storage in methanol, notable bleaching of RhB is observed. In comparing Figures 7(d) and (e), the photocatalytic activity is more easily saturated for 30 days stored Si QDs than for 10 days stored ones. Our analyses revealed that longer period storage of Si QDs in methanol affects mainly the reaction saturation and less the reaction rate[79]. This suggests that charge neutralization process, which is required after electron transfer from a Si QD to RhB to neutralize the Si QD, is more sensitive to the tunnelling barrier thickness than the electron transfer process.

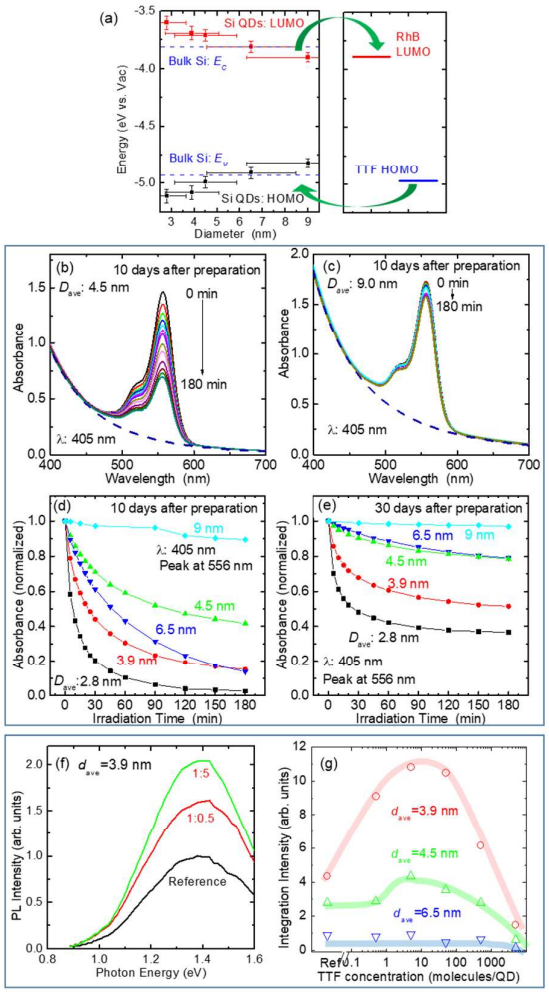

Figure 7 (a) HOMO and LUMO levels with respect to the vacuum level of Si QDs with different sizes. The LUMO of RhB (-3.88 eV) and the HOMO of TTF (-4.97 eV) is shown in the right panel. (b)(c) Progression of absorption spectra of Si QDs-RhB mixture solutions under light irradiation (405 nm); (b) 4.5 and (c) 9.0 nm in diameters. Dashed lines are absorption spectra of Si QDs solutions without RhB. (d)(e) Normalized absorbance of RhB (at 556 nm) as a function of irradiation time. The size of Si QDs is changed from 2.8 to 9 nm. The data are obtained for Si QDs stored in methanol for (d) 10 days and (e) 30 days. (f) PL spectra of Si QDs 3.9 nm in diameter in mixture solutions of Si QDs and TTF. The molar ratio of TTF to a Si QD is changed. (g) Integral PL intensity of Si QDs with different diameters as a function of TTF/Si QDs molar ratio. (b-e) Reproduced from Ref. [79]. Copyright 2018 American Chemical Society. (f, g) Reproduced from Ref. [81]. Copyright 2017 American Chemical Society.

By choosing proper molecules, charge transfer interaction between Si QDs and molecules enhances the PL of Si QDs [81]. We studied the interaction between Si QDs and tetrathiafulvalene (TTF), which has the HOMO near that of Si QDs (Figure 7(a)) and can act as an electron donor to Si QDs. Figure 7(f) shows PL spectra of a mixture solution (methanol) of Si QDs and TTF. The average diameter of Si QDs is 3.9 nm. The molar ratio of TTF to a Si QD is changed. The black curve is the PL spectrum of a Si QDs solution without TTF. The PL intensity increases by adding TTF; the intensity is doubled when the ratio is 5. The observed PL enhancement can be

explained by the electron transfer from an adsorbed TTF molecule to a "dark" Si QD having electron traps and resultant inactivation of the traps, which converts a "dark" Si QD to a luminescing "bright" one [81]. Note that the PL intensity returns to the reference level if TTF is removed from a mixture solution by centrifugation. Similar PL enhancements are observed for other molecules acting as electron donors.

In Figure 7(g), the integral PL intensities are plotted as a function of the TTF/Si QDs ratio for different size Si QDs. In Si QDs 3.9 and 4.5 nm in diameter, the intensity first increases, reaches a maximum around TTF/QD = 5, and then decreases, while in Si QDs 6.5 nm in diameter, no increase of the intensity is observed. The observed size dependence can also be explained by the model similar to the case of RhB. Electron transfer from TTF to Si QDs is expected to be the most efficient for the smallest Si QDs (3.9nm in diameter) because of the large energy difference between HOMOs of Si-QDs and TTF (Figure 7(a)). The rate decreases in slightly larger Si QDs (4.5 nm in diameter) because the HOMO levels almost coincide. For the largest Si QDs, the electron transfer is prohibited, and thus no PL change is observed.

Energy transfer. Besides charge transfer interactions, Si QDs interact with other materials via a long-range Förster resonant energy transfer (FRET). In particular, sensitized excitation of rare-earth ions such as Er^{3+}, Yb^{3+}, Tm^{3+}, etc., by Si QDs has widely been studied[82-85]. FRET does not require direct overlap of wavefunctions and thus constraint to the surface structure is relaxed compared to charge transfer. For the last decade, FRET between Si QDs has been attracting significant attention, because it may improve the performance of Si QDs-based solar cells via FRET mediated multiple exciton generation [86-88]. However, direct evidence of FRET between Si QDs was very scarce, and FRET was usually discussed by analysing the PL decay curves under several assumptions [86-90]. It turned out from detailed theoretical studies that efficient FRET between Si QDs occurs only when they are almost in contact [91-94], the condition of which is not fulfilled in majority of Si QDs samples.

From a colloidal solution of codoped Si QDs, a dense film or a solid of Si QDs can be produced by spin-coating or drop-casting [95-97]. Figure 8(a) shows a TEM image of a monolayer of codoped Si QDs [97]. Because of the ligand-free surface, Si QDs are attached each other. Efficient FRET is thus anticipated. To study FRET between Si QDs, we prepare solutions of Si QDs with different size distributions as shown in Figure 8(b). The absorption and PL spectra are shown in Figure 8(c). Signatures of FRET can be readily observed if we simply compare the PL spectra and decay dynamics between a Si QDs solution and the solid [95]. We compare PL properties of a solid and a solution for two samples with different average sizes, *i.e.*, 3 nm and 6.8 nm, in Figure 8(b). In both cases, in a QDs solid, the PL peak shifts to lower energy compared to that of a QDs solution and the decay time becomes shorter, especially at the high energy side of the PL band [95]. These changes can be explained by energy transfer from smaller to larger Si QDs within the size distribution in a dense QDs solid. The signature of energy transfer becomes more prominent when the size distribution is intentionally broadened by mixing solutions of Si QDs with large and small average sizes in Figure 8(b), especially when the mixing ratio of the solution of large Si QDs is increased. In the solid made from the mixed solution, the PL spectral shape is totally different from that of the solution due to efficient energy transfer in the solid [95]. The observed effect is explained by the increase of a number of acceptor QDs per a donor QDs in the broadened size distribution.

In order to quantitatively discuss the energy transfer rate and the efficiency, we produced the structures summarized in Figure 8(d) [97]. The structure "B" is a monolayer of Si QDs, and "D" is the double layer separated by a thin polymer layer (~0.45 nm) grown by a layer-by-layer (LbL) assembly process. The structure "C" is a monolayer of Si QDs prepared by a mixture solution. The structure "E" is a multilayer prepared by depositing monolayers of different size Si QDs. The spacer thickness is ~0.45 nm. Finally, the structure "F" is a multilayer film similar to "E", but the spacer thickness is larger (1.35 nm). Figure 7(e) shows the energy transfer rate estimated from the PL decay rates for these structures. We can clearly see that the energy transfer rate increases from one pair of different size monolayers (E-$(3.0/6.8)_{1/1}$) to the two pairs (E-$(3.0/6.8)_{2/2}$). This is explained by the increased chance of finding large Si QDs (energy acceptor) for a small QD (energy donor) in "E-$(3.0/6.8)_{2/2}$" than in "E-$(3.0/6.8)_{1/1}$". The increase of the energy transfer rate from the two pairs (E-$(3.0/6.8)_{2/2}$) to the three pairs (E-$(3.0/6.8)_{3/3}$) is very small, indicating that the energy transfer is possible only between neighbouring layers. The energy transfer rate decreases when the separation between the layers increases. We also estimated the Förster radius (~4.9 nm) and the energy transfer efficiency [97]. All the results are consistent with the theoretical predictions that Si QDs should be almost in contact for efficient energy transfer [91-94].

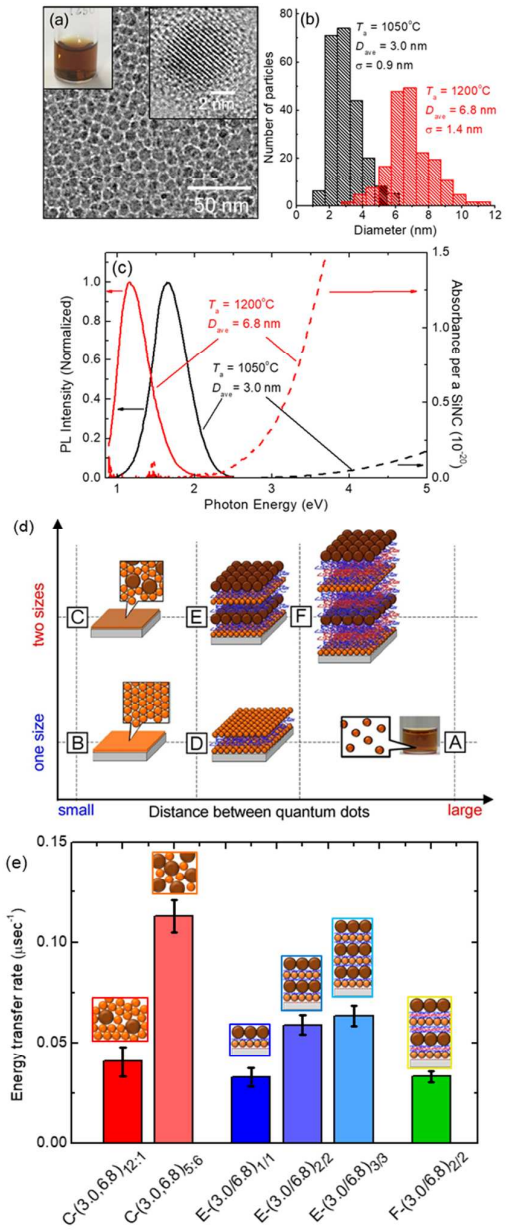

Figure 8 (a) TEM image of a monolayer of Si QDs grown at 1200°C. (b) Size distribution of Si QDs grown at 1050 and 1200°C. (c) Normalized PL spectra and absorbance spectra of Si QDs dispersed in methanol. (d) Schematic illustrations of Si QD assemblies. "A" is a colloidal dispersion. "B" is a QD solid made from nominally one size QDs. "C" is a QD solid made from two different size QDs. "D", "E" and "F" are LBL assemblies. "D" is composed of one size QDs, while "E" and "F" are composed of QDs with two different sizes. The inter-layer distance in "F" is larger than that in "E". From left to right, the average separation between QDs increases. (e) Energy transfer rates of Si QD assemblies with different configurations in (d). (d, e) Reproduced from Ref. [97]. Copyright 2016 American Chemical Society.

Si QDs-based composites

Immobilization on substrate. For the application of codoped Si QDs in optoelectronic and biophotonic devices, the immobilization on a substrate via covalent bonds is necessary. We have developed several processes to immobilize codoped Si QDs on silica, silicon [98] and Au [28] surface. Figure 9(a) shows the process to immobilize Si QDs on a silica substrate. First, the surface of codoped Si QDs is functionalized with allylamine (AAm) by the hydrosilylation reaction. A SiO_2 substrate modified with 3-glycidyloxypropyltrimethoxysilane (GOPTS) self-assembled monolayer (SAM) is then immersed in the solution of AAm-functionalized Si QDs. The reaction between the amines on the surface of Si QDs and the epoxy group results in the immobilization. Figure 9(b) shows the similar process by using Si QDs functionalized with acrylic acid (AAc) and a (3-aminopropyl) trimethoxysilane (APTMS) SAM modified Si substrate. Figure 9(f) shows an atomic force microscope (AFM) image of a SiO_2 substrate after the process in Figure 9(a). Figure 9(c-e) is the control; (c) a SiO_2 substrate. (d) a SiO_2 substrate with GOPTS SAM immersed in distilled water, and (e) that immersed in the solution of untreated codoped Si QDs. The image in Figure 9(f) and the height profile in Figure 9(g) indicate that Si QDs are immobilized on the substrate in the process in Figure 9(a).

It is important to note that in both AAm and AAc-functionalized codoped Si QDs, the PL spectral shape is almost unaffected by the process. This is a stark contrast from conventional organic-capped Si QDs. In organic-capped Si QDs, the PL spectrum is very sensitive to the kinds of ligands and the luminescence color changes from blue to NIR easily [3, 99]. We believe that the shell is responsible for the very robust luminescence of codoped Si QDs; the shell prevents penetration of electron and hole wavefunctions to the surface. In AAc-functionalized Si QDs, the PL intensity increased by the functionalization process due probably to the suppression of surface defects. In AAm-functionalized case, on the other hand, the PL intensity decreased. This is probably due to the damage on the surface of Si QDs induced during the process in high pH solutions (pH>12).

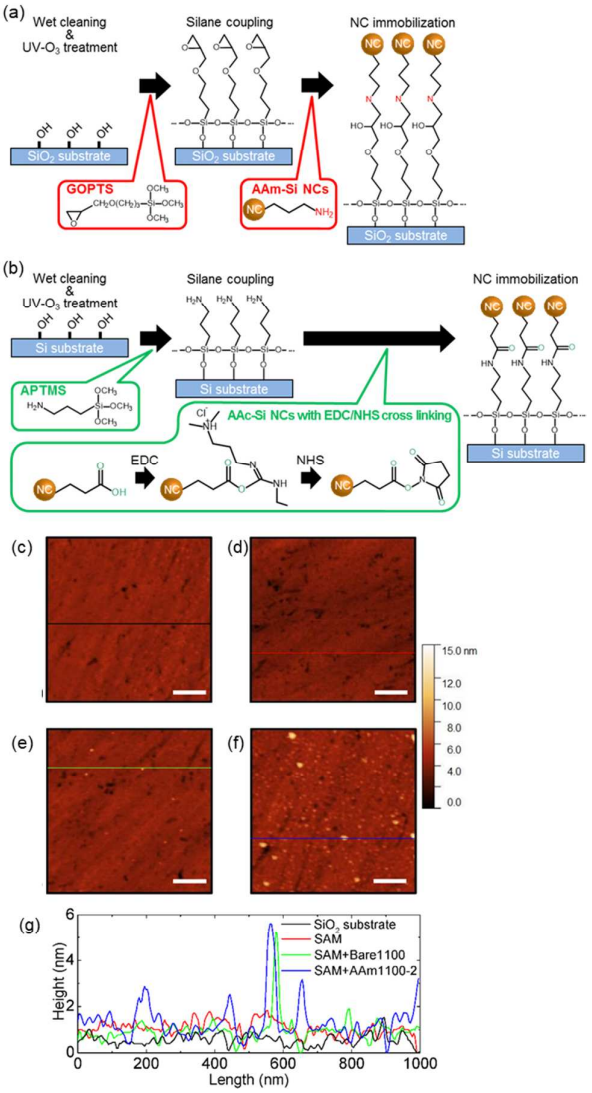

Figure 9 (a) Protocol for immobilization of AAm-Si QDs on a SiO_2 substrate. (b) Protocol for immobilization of AAc-Si QDs on a Si substrate. (c) AFM topography image of a SiO_2 substrate. (d-f) SiO_2 substrates with GOPTS SAM immersed in (d) distilled water, (e) untreated codoped Si QDs solution, and (f) AAm-functionalized codoped Si QDs solution. The scale bar represents 200 nm. (g) Height profiles at the positions marked in the topography images. Each profile is obtained by subtracting the lowest height as an offset value from the measured height. Reproduced from Ref. [98]. Copyright 2016 Materials Research Society.

Si QDs/polymer composite. Si QDs can be dispersed in a variety of polymers[20-24] and composites with very high PL QY (65%) are produced [24]. We produced a composite of codoped Si QDs and water-based hydroxypropyl cellulose (HPC) polymer as a bio-compatible NIR light emitter. The preparation procedure is very simple. HPC is dissolved in methanol and mixed with a methanol solution of Si QDs. Drop-casting of the mixture solution on a substrate results in the formation of a composite film[25]. The left-top image in Figure 10(a) is a photograph of a HPC film in which Si QDs are dispersed under UV irradiation (~365 nm) [25]. The emission is coupled with the waveguide modes of the substrate and out-coupled at the edge. As a result, the top emission is very weak. This proves the high flatness of the composite film. Similar edge-emission is observed in a Si QDs solid on a silica substrate (right-top image). In this case the top emission is even smaller. The HPC film can easily be peeled off from the substrate. The left-bottom image is a peeled Si QDs/HPC composite film. By bending, we can see bright emission from the surface.

In addition to a flat composite film, we can produce a highly scattering xerogel film of the composite, in which submicrometer size pores are dispersed, by simply changing the composition of the mixture solution. The right-bottom image in Figure 10(a) is a picture of a xerogel film (~1 μm in thickness) under UV irradiation[25]. Due to strong scattering by the pores, the luminescence extraction efficiency is strongly enhanced and a strong top emission is observed. Because of the multiple scattering by the pores, the effective absorption cross section of embedded Si QDs is 30-40 folds enhanced in a green-red wavelength range. This can be seen in the strong enhancement of the light extinction in the xerogel film in Figure 10(b). We found that due to the enhancements of the excitation efficiency and the extraction efficiency, PL from the top surface is at maximum 40 folds enhanced in the xerogel film compared to a smooth Si QDs film [25].

An advantage of the Si QDs/HPC composite is that the shape can be controlled very easily. We can produce a nanofiber of the composite by electrospinning[19]. Figure 10(c) shows a scanning electron microscope (SEM) image of HPC nanofibers produced by electrospinning [19]. In the nanofiber, Au NPs and Si QDs are dispersed. They can be seen in the TEM images in Figure 10(d) and (e), respectively. Figure 10(f) shows a micro-PL image of a composite nanofibers under 430 nm excitation. Due to the scattering by Au NPs, the bright emission from Si QDs can be observed from the surface of the nanofibers.

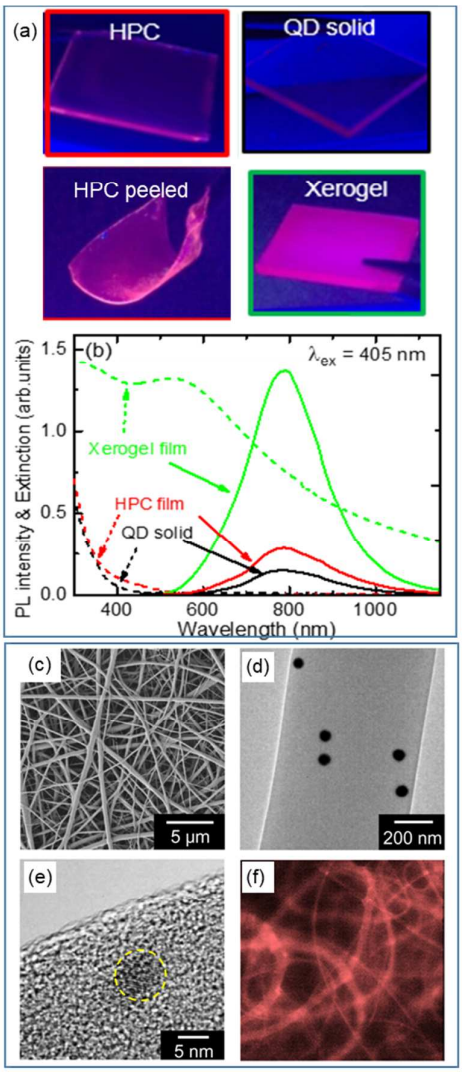

Figure 10 (a) Photographs of a flat HPC film containing Si QDs on silica substrate (top-left) and that peeled off from the substrate (bottom-left) under UV irradiation. (top-right) Si QDs solid on silica substrate and (bottom-right) HPC xerogel film containing Si QDs on silica substrate under UV irradiation. The average diameter of Si QDs is 2.8 nm. (b) PL (solid curve) and PLE (dashed curve) spectra of the samples in (a). (c) SEM image of electrospun HPC nanofibers doped with Si QDs and Au NPs. (d) and (e) TEM images showing Au NPs and a Si QD in a nanofiber, respectively. (f) Microscope PL image of a HPC nanofiber containing Si QDs and Au NPs[19]. (a-b) Reproduced from Ref. [25]. Copyright 2017 American Chemical Society. (c-f) Reproduced from Ref. [19]. Copyright 2015 AIP Publishing LLC.

Si QDs/metal composite. In Si QDs/polymer composites, the role of polymer is almost solely the host to provide the mechanical strength and to define the macroscopic shape to manipulate incoming and emitted light. On the other hand, in Si QDs/metal nanostructure composites, coupling of the excitonic states of Si QDs and surface plasmons in metal nanostructures modifies the optical response of Si QDs significantly. We have produced many kinds of Si QDs/metal nanocomposites by different processes. Some of them are summarized in Figure 11. The simplest method for the formation of Si QDs/metal nanocomposites is utilizing the electrostatic attraction. Since the surface of codoped Si QDs is negatively charged, simple mixing of a solution of codoped Si QDs and that of positively charged metal nanostructures results in the formation of a nanocomposite. The Si QDs/Au NP nanocomposite in Figure 11(a) is produced by the procedure[27]. The surface of Au NP is covered by poly(allylamine hydrochloride) (PAH) to make the surface positively charged. In the nanocomposites, we observed the enhancement of the excitation cross-section of Si QDs PL around the resonance wavelength of localized surface plasmons of Au NPs (~540 nm)[27]. Similarly, nanocomposites of Si QDs and Au nanorods can be prepared by using the electrostatic attraction. Figure 11(b) and (c) shows the TEM images[26]. Si QDs are separated from the Au nanorod surface about 8.7 nm by a polymer layer. In Ref. [26], the aspect ratio of Au nanorods was chosen so that the localized surface plasmon resonance (LSPR) wavelength overlaps with the PL wavelength of Si QDs. We observed enhancement of the decay rate and the QY at the LSPR wavelength. The enhancement factor of the QY due to the Purcell effect was estimated to be ~3. The PL was polarized to the direction of the long axis of a Au nanorod.

Although the process to use electrostatic attraction is very simple, the controllability of the structure is not high. We developed a process to make composites by chemical bonding. Figure 11(d-f) shows one of the results [28]. In this case, codoped Si QDs are functionalized with (3-mercaptopropyl)trimethoxysilane. Since thiol group forms chemical bonds with Au, nanocomposites are formed spontaneously by simply mixing aqueous solution of thiol functionalized Si QDs with citrate-stabilized Au NPs. In this method, a monolayer of Si QDs is formed on the surface of a Au NP as can be seen in the TEM images (Figure 11(d) and (e)) and the EDS mapping image (Figure 11(f)). A drawback of this method is the very short distance between a Si QD and Au surface for LSPR mediated PL enhancement.

We developed a process to use DNA molecules as a spacer to control the distance very precisely [28]. Figure 11(g) shows the scheme. Si QDs functionalized with 3-ethoxydimethylsilyl)propylamine and carboxyl-modified single strand DNA (ssDNA) is conjugated by peptide bonding using 4-(4,6-dimethoxy-1,3,5-triazin-2-yl)-4-methylmorpholium chloride (DMT-MM) as a condensing agent[28]. The Si QDs are then annealed with Au NPs having the complementary ssDNA in hybridization buffer. Figure 11(h) and (i) shows TEM images of a Si QDs/Au NP nanocomposites prepared by this method. The EDS mapping is shown in Figure 11(j). In Figure 11(i), we can see that Si QDs and Au surface is separated by 10 nm, which corresponds to the length of the DNA. Therefore, the designed structure is fabricated by the process [28].

In the above mentioned processes, Si QDs and metal nanostructures are prepared in advance and then merged. We also developed a totally new self-limiting synthetic process of a nanocomposite [100]. The method uses reactive surfaces of freshly-prepared H-terminated codoped Si QDs. For the preparation of Si QDs/Au NP composites, simply a methanol solution of hydrogen tetrachloroaurate (III) tetrahydrate ($HAuCl_4 \cdot 4H_2O$) is added to a methanol solution of a H-

terminated codoped Si QDs. Figure 11(k) and (l) are a TEM image and a EDS mapping image of a nanocomposite, respectively. $HAuCl_4$ is reduced by Si QDs and a small Au NP is grown. The growth of the Au NP is stopped when the surface is fully covered by Si QDs. The size of Au NPs can be controlled in a very wide range by simply changing the mixing ratio of Si QDs and $HAuCl_4$. With this process, surprisingly uniform structures are produced and they are perfectly dispersed in methanol. Therefore, by spin-coating the solution on a substrate, a film of Au NPs with controlled separations can be prepared. By exactly the same procedure, Si QDs/Ag NP composites (Figure 11(m) and (n)) and Si QDs/Au NP/Ag NP composites can be produced. In the case of Pt, the structure of nanocomposites is different (Figure 11(o) and (p)). Very small Pt NPs (~1.5 nm in diameter) are grown on the surface of Si QDs.

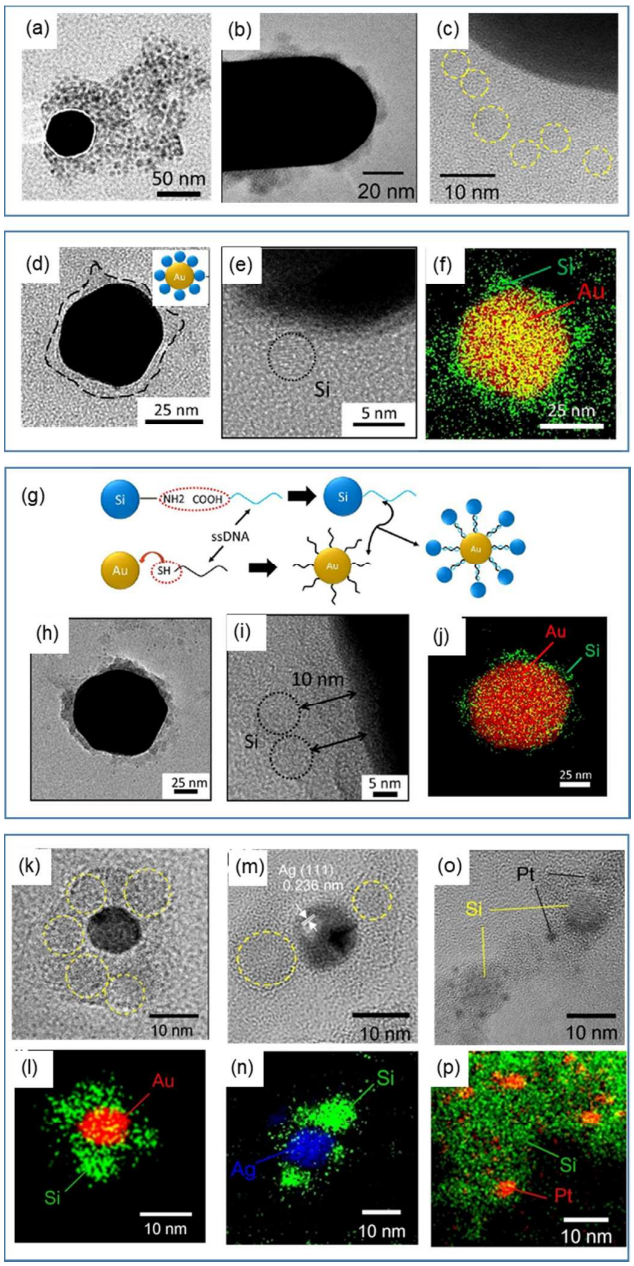

Figure 11 (a-c) TEM images of Si QDs/Au NP composites made by electrostatic attraction between Si QDs and a Au NP (a) and a Au nanorod (b, c). (d-f) TEM images of Si QDs/Au NP composites made by covalent bonds (d, e) and the EDS mapping image (f). (g) Scheme to produce Si QDs/Au NP composite by DNA hybridization. (h-j) TEM images of Si QDs/Au NP composites made by DNA hybridization (h, i) and the EDS mapping image (j). (k-p) TEM images and EDS mapping images of nanocomposites produced by reducing metal salts by Si QDs. (k, l) Si QDs/Au NP composites, (m, n) Si QDs/Ag NP composites, and (o, p) Si QDs/Pt NP composites. (a) Reproduced from Ref. [27]. Copyright 2015 American Chemical Society. (b, c) Reproduced from Ref. [26]. Copyright 2015 American Chemical Society. (d-j) Reproduced from Ref. [28] with permission from The Royal Society of Chemistry. (k-p) Reproduced from Ref. [100] with permission from The Royal Society of Chemistry.

Si QDs on plasmonic substrate. Besides Si QDs/metal nanocomposites, we study the coupling of the emission of Si QDs with a variety of plasmonic substrate. The research on the

coupling between Si QDs and surface plasmons on flat/rough metal surfaces was first conducted for Si QDs layers produced by ion implantation [101-103] and then for those produced by sputtering [104-106]. In these techniques, distribution of Si QDs density in the depth direction is inevitable and it smears the effect of the coupling. In Ref. [107] and [108], We demonstrated that by using a Si QDs monolayer produced from the colloidal solution, the effect appears more clearly. Figure 12(a) shows one of the structures studied. A monolayer of Si QDs is placed on a Ag film-over nanosphere plasmonic structure via a precisely thickness controlled polymer layer[107, 109]. The structure has several surface plasmon resonance peaks in the visible to NIR ranges, and thus simultaneous enhancements of the excitation and emission processes, *i.e.*, double resonances, are possible. We observed strong modifications of the PLE and PL spectral shape [57]. In the wavelength range where the intrinsic absorption cross section of Si QDs is small, *i.e.*, yellow to red regions, the PL enhancement factor reaches 12[57]. The enhancement of the absorption cross section in the long wavelength range is very important for the biophotonics applications. We observed similar effects for plasmonic substrates produced by nanoimprint lithography (Figure 12(b))[108]. Due to the strong modification of the spectral shape and the decay rate of a Si QDs monolayer by a plasmonic substrate, it can be used as a probe to determine the Purcell enhancement factor of a plasmonic substrate[109].

We also study the coupling of Si QDs with gap surface plasmons in a metal nanoparticle on mirror (MNPoM) structure shown in Figure 12(c). In the MNPoM structure, a metal NP is placed on a metal thin film with a gap of a few nanometers. Because of the coupling of the surface plasmon polaritons (SPPs) of a metal film with localized surface plasmons (LSPs) of a metal NP, a very strong electric field is induced in the gap. The gap plasmons enhance optical responses of materials in the gap. In Figure 12(c), we use a monolayer of Si QDs as a light emitting material as well as a spacer that determines the gap length very precisely. Figure 12 (d) shows the PL spectra [110]. In the gold nanoparticle on a gold mirror (AuNPoM) structure, the intensity of PL from a Si QDs monolayer (red) is strongly enhanced compared to that on a Au thin film (blue). Furthermore, the PL spectral shape is strongly modified from that on a silica substrate. The spectral shape coincides almost perfectly with the scattering spectra of the same AuNPoM structure. This indicates coupling of the emission of a Si QDs monolayer with the gap plasmon mode.

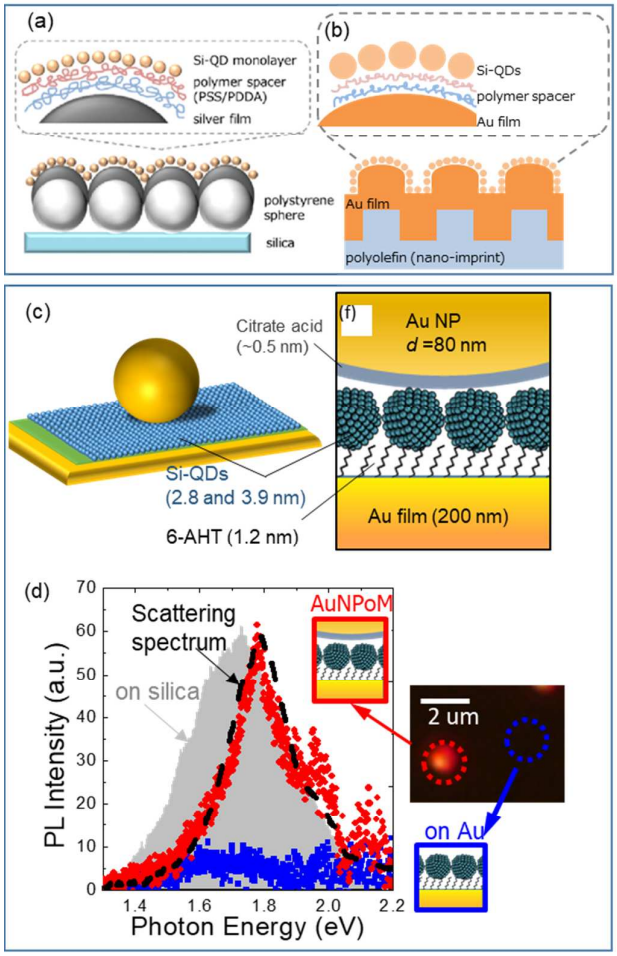

Figure 12 (a, b) Schematic illustrations of plasmonic substrates made by nanosphere lithography (a) and nanoimprint lithography (b), on which a monolayer of Si QDs are placed. (c) Schematic illustration of Au NP on mirror structure. A monolayer of Si QDs is placed in the nanogap. (d) PL spectra of a monolayer of Si QDs in a AuNPoM structure and on a Au flat film. PL spectrum on a silica substrate is also shown. Dashed curve is the scattering spectrum of the same structure. Scattering image is shown on the right side. (a) Reproduced from Ref. [107]. Copyright 2017 American Chemical Society. (b) Reproduced from Ref. [108]. Copyright 2017 AIP Publishing LLC. (c-d) Reproduced from Ref. [110]. Copyright 2016 American Chemical Society.

Current transport properties

We now turn our attention to the current transport properties of Si QDs thin films produced from a colloidal solution of codoped Si QDs. In undoped and solely B or P doped Si QDs, the current transport properties have been studied in detail[111-113] and electronic devices such as thin film transistors (TFTs)[111, 114], light-emitting diodes (LEDs)[15, 115-118] and solar cells[119] are developed. On the other hand, the study on the current transport properties of codoped Si QDs is still limited. The conductance of a codoped Si QDs film depends strongly on the surface structure. The conductivity of a film produced from H-terminated fresh Si QDs is around 10^{-5} S/cm, while that from Si QDs aged in methanol for more than a month is below 10^{-11} S/cm. By using H-terminated Si QDs, we are now producing several devices including TFTs and photodetectors. Although

we observe the transistor operation and the photocurrent, the performance is not satisfactory due mainly to the poor carrier mobility. Development of technology to improve the carrier mobility is indispensable to realize practically useful devices from codoped Si QDs. As one of the approaches, we are developing a process to bridge Si QDs by metal ions [120].

In contrast to H-terminated fresh Si QDs, in a film produced from the solution of aged O-terminated Si QDs, proton transport in water molecules adsorbed on the surface of Si QDs dominates the charge transport as schematically shown in Figure 13(a). Therefore, the conductivity depends strongly on the amount of adsorbed water molecules. Depending on the amount of water molecules, the conductivity changes 8 orders of magnitude [96]. We analysed the transport mechanism by the impedance spectroscopy as well as the DC transport measurements [121].

Because of the high sensitiveness of the conductivity on the vapor pressure, Si QDs film can be used as a humidity sensor for monitoring human respiration and water evaporation on skin [122]. We prepared the sensor chip by spin-coating a colloidal solution of Si QDs on an inter-digitated electrode made on a polyimide film as schematically shown in Figure 13(b). In Figure 13(b), an AFM image of a Si QDs film drop-casted on a fused silica substrate is also shown. A very flat and dense film is produced. A device in Figure 13(b) is a portable respiration sensor, which consists of a signal processor and a headset with a sensor chip[123]. In Ref. [123], we used SiO_2 NPs not Si QDs as a material for the sensor chip. However, there are no differences on the sensor properties between them. Figure 13(c) shows the output signal of the portable respiration sensor in different respiration patterns. The speed and intensity of respiration are intentionally changed. The distance between the sensor and a human face is approximately 5 cm and exhaled air from the nose is given to the sensor. The sensor monitors all possible respirations patterns.

We also produced several other kinds of devices by using aged O-terminated Si QDs. One of them is a resistive switching memory. We observed reproducible resistive switching of a Si QDs film sandwiched by two electrodes. Our analysis suggests that the switching is due to the formation and destruction of a conductive filament of oxygen vacancies on Si QD surface by an electric field. We also produced a single electron transistor by placing a Si QD, which acts as a Coulomb island, on nanogap metal electrodes [124]. Si QDs can also be used as a floating gate. We developed a process to embed codoped Si QDs in a HfO_x thin film in metal-insulator-semiconductor (MIS) structure and studied the capacitance-voltage property [125].

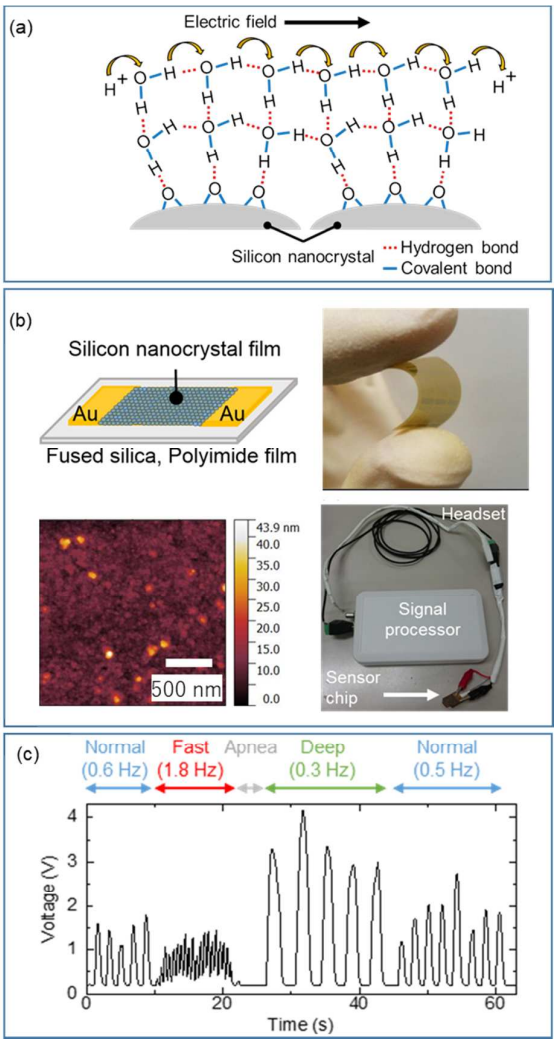

Figure 13 (a) Proton transport on O-terminated Si QDs. (b) Portable respiration sensor consisting of a signal processor and a headset with a sensor chip, schematic illustration of a sensor chip, picture of a sensor chip (polyimide substrate), and AFM topographic image of a Si QDs film drop-casted on a silica substrate. (c) Voltage output in different respiration patterns. The data are obtained for a SiO_2 NPs film sensor. (a) Reproduced from Ref. [122]. Copyright 2017 American Chemical Society. (b, c) Reproduced from Ref. [123]. Copyright 2018 IEEE.

Fluorescence bioimaging

As mentioned several times in this article, codoped Si QDs have several desirable properties for biosensing and bioimaging. We demonstrated in vitro imaging of human osteoblasts by codoped Si QDs and performed the evaluation of the cytotoxicity [39, 126]. Figure 14(a) shows a fluorescence microscope image of human osteoblasts cultivated in a medium containing codoped Si QDs (excitation wavelength: 405 nm). The green layer corresponds to the full signal and the red one corresponds to that above 785 nm. From the fluorescence spectra in Figure 14(b), the green layer is dominated by autofluorescence, while the red one is dominated by the luminescence from Si QDs. The luminescence spectrum in the cell is almost identical with that

of a Si QDs solution. The luminescence is stable in the cells for more than 24 hours.

In Figure 14, we use Si QDs luminescing in a red region. The contrast between the fluorescence signal and autofluorescence is further improved if we bring the emission wavelength to so-called second window of biological tissue (1000-1350nm)[127]. We are now developing a process to improve the luminescence QY of codoped Si QDs above 1000 nm. Another important technology to improve the fluorescence image contrast is the time-gated imaging [128]. Since the luminescence lifetime of codoped Si QDs is very long (several tens of μs)[2], they are very suitable for time-gated imaging. In vivo time-gated fluorescence imaging was demonstrated for porous Si NPs [129].

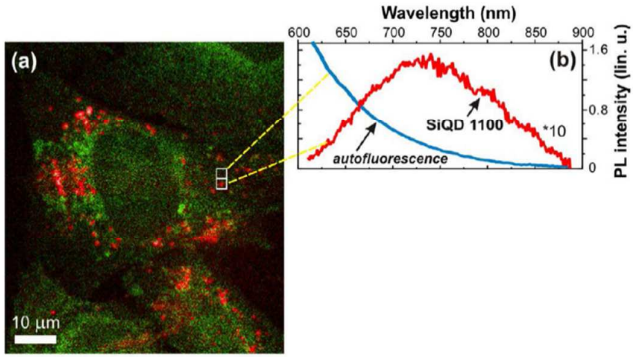

Figure 14 Fluorescence microscopy and spectroscopy under 405 nm (CW) excitation for human osteoblasts cultivated in a medium with codoped Si QDs. (a) Combined fluorescence image with the green layer showing the full signal (dominated by cell autofluorescence) and the red layer showing signal above 785 nm (dominated by Si QDs PL). (b) PL spectrum of cell autofluorescence (blue) and PL of Si QDs (red) from areas indicated by rectangles in (a). Reproduced from Ref. [39] with permission from The Royal Society of Chemistry.

Dielectric nanoantenna

From now on, we focus on a unique and important dielectric property of Si NCs. Crystalline Si has a large real part and a small imaginary part of the permittivity in a wide wavelength range covering the whole visible to NIR ranges due to the indirect nature of the energy band structure. A sub-quarter μm size NP of crystalline Si supports the lowest order Mie resonances *i.e.*, the magnetic dipole (MD) and electric dipole (ED) resonances, in the visible to the NIR ranges [130], and acts as a new type of low-loss nanoantenna. However, the production process of sub-quarter μm crystalline Si NPs, especially the colloidal solution, is not established. It is important to note that "crystalline" is crucial, because a large imaginary part of the permittivity in amorphous Si ruins the property as a low-loss Mie resonator.

As shown in Figure 1(c), we have succeeded in producing a colloidal solution of sub-quarter μm size crystalline Si NPs [33]. Figure 15(a) shows a dark-filed scattering image of Si NCs on a silica substrate prepared by drop-casting the colloidal solution [33]. Colourful dots due to the scattering of Si NCs can be seen in the whole region. Figure 15(b) shows a magnified image and Figure 15(c) shows a SEM image of the same area. The comparison of these images confirms that the colour arises from single Si NCs. Figure 15(d-h) shows forward and backward scattering spectra of individual Si NCs. The corresponding scattering and SEM images are shown in the inset. Figure 15(i–m) shows the calculated forward (black solid lines) and backward (red dashed lines) scattering cross-section spectra of a Si sphere with the diameters obtained from SEM images in Figure 15(d–h), respectively. The calculation is based on the Mie theory which provides the exact solution of the light scattering by a sphere. We can see very good agreement between the measured and calculated scattering spectra. The longest wavelength mode is the MD Mie resonance and the second longest wavelength mode is the ED Mie resonance. These modes shift to higher energy with increasing the size.

The Mie resonances induce strong electric fields on the surface of Si QDs, which enhance the optical responses of a nearby material. We studied PL of a very thin RhB layer by the geometry in Figure 15(n), and observed the strong enhancement (Figure 15(o)) [33]. The enhancement factor reaches at maximum 200-fold. It should be stressed here that the enhancement is achieved just by placing a Si NC on a dye layer without any control of the emitter-NC distance. This is not possible in plasmonic nanostructures, where accurate control of the distance is crucial to achieve the enhancement.

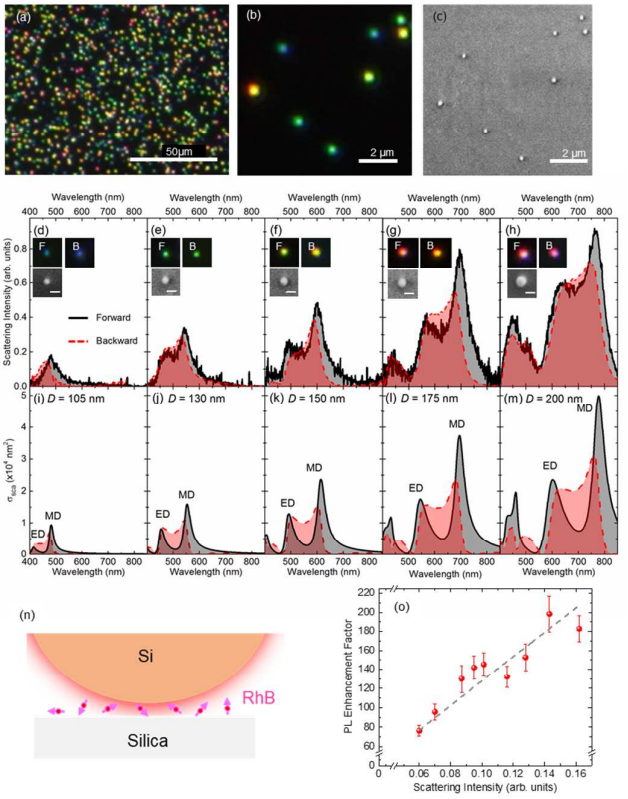

Figure 15 (a) Dark-field scattering image of Si NCs on a silica substrate. (b) Higher magnification dark-field and (c) SEM images of Si NCs taken at the same region on a silica substrate. d–h) Measured scattering spectra in forward (black solid lines) and backward (red dashed lines) directions from single Si NCs. Insets show the forward (F) and backward (B) scattering and SEM images of corresponding Si NCs. (i–m) Calculated forward and backward scattering cross-section spectra for Si NCs with the diameters estimated from SEM images in (d–h), respectively. n) Schematic illustration of the structure for the enhancement of RhB luminescence by a Si NC. (o) Relation between

the enhancement factor of PL from RhB and the scattering intensity of single Si NCs. Reproduced from Ref. [33]. Copyright 2017 Wiley-VCH Verlag GmbH & Co.

In the structure shown in Figure 15(n), the field enhancement arises solely from the Mie resonance of a Si NC and the effect of silica substrate is negligible. On the other hand, if we place a Si NC on metal, a dielectric-metal hybrid nanogap resonator can be produced. We observed much larger field enhancement and resultant PL enhancement by the nanogap structure [131].

Summary

In summary, in the first half of this article, we discussed the structure and the fundamental physical properties of B and P codoped Si QDs, and in the second half, we mainly discussed the interaction of codoped Si QDs with other materials, especially the formation of Si QDs-based nanocomposites. Thanks to a heavily B and P codoped shell, which protects a Si QD core from the environment, the luminescence property is extraordinary immune compared to conventional Si QDs. This feature in combination with other characteristic features such as high dispersibility in water makes codoped Si QDs very unique and attractive in many fields. We believe that codoped Si QDs and NCs can be a functional building blocks for a variety of new environmentally friendly sensing and energy harvesting devices.

Acknowledgements

This work was partly supported by the 2015 JST Visegrad Group (V4) – Japan Joint Research Project on Advanced Materials and JSPS KAKENHI Grant Number 16H03828.

Conflicts of interest

There are no conflicts to declare.

Notes and references

1. M. L. Mastronardi, F. Maier-Flaig, D. Faulkner, E. J. Henderson, C. Kubel, U. Lemmer and G. A. Ozin, *Nano Lett.*, 2012, **12**, 337-342.
2. H. Sugimoto, M. Fujii, K. Imakita, S. Hayashi and K. Akamatsu, *J. Phys. Chem. C*, 2013, **117**, 11850-11857.
3. M. Dasog, G. B. De los Reyes, L. V. Titova, F. A. Hegmann and J. G. Veinot, *ACS Nano*, 2014, **8**, 9636-9648.
4. X. Liu, Y. Zhang, T. Yu, X. Qiao, R. Gresback, X. Pi and D. Yang, *Particle & Particle Systems Characterization*, 2016, **33**, 44-52.
5. Y. Yu, G. Fan, A. Fermi, R. Mazzaro, V. Morandi, P. Ceroni, D.-M. Smilgies and B. A. Korgel, *J. Phys. Chem. C*, 2017, **121**, 23240-23248.
6. F. Erogbogbo, K.-T. Yong, I. Roy, G. Xu, P. N. Prasad and M. T. Swihart, *ACS Nano*, 2008, **2**, 873-878.
7. F. Erogbogbo, K. T. Yong, I. Roy, R. Hu, W. C. Law, W. Zhao, H. Ding, F. Wu, R. Kumar, M. T. Swihart and P. N. Prasad, *ACS Nano*, 2011, **5**, 413-423.
8. H. Jaganathan and B. Godin, *Adv. Drug Deliv. Rev.*, 2012, **64**, 1800-1819.
9. S. Bhattacharjee, I. M. Rietjens, M. P. Singh, T. M. Atkins, T. K. Purkait, Z. Xu, S. Regli, A. Shukaliak, R. J. Clark, B. S. Mitchell, G. M. Alink, A. T. Marcelis, M. J. Fink, J. G. Veinot, S. M. Kauzlarich and H. Zuilhof, *Nanoscale*, 2013, **5**, 4870-4883.
10. R. J. Clark, M. Aghajamali, C. M. Gonzalez, L. Hadidi, M. A. Islam, M. Javadi, M. H. Mobarok, T. K. Purkait, C. J. T. Robidillo, R. Sinelnikov, A. N. Thiessen, J. Washington, H. Yu and J. G. C. Veinot, *Chem. Mater.*, 2017, **29**, 80-89.
11. M. H. Mobarok, T. K. Purkait, M. A. Islam, M. Miskolzie and J. G. C. Veinot, *Angew. Chem.*, 2017, **129**, 6169-6173.
12. F. Sangghaleh, I. Sychugov, Z. Yang, J. G. C. Veinot and J. Linnros, *ACS Nano*, 2015, **9**, 7097-7104.
13. J. G. Veinot, *Chemical communications*, 2006, DOI: 10.1039/b607476f, 4160-4168.
14. L. Mangolini and U. Kortshagen, *Adv. Mater.*, 2007, **19**, 2513–2519.
15. M. L. Mastronardi, E. J. Henderson, D. P. Puzzo, Y. Chang, Z. B. Wang, M. G. Helander, J. Jeong, N. P. Kherani, Z. Lu and G. A. Ozin, *Small*, 2012, **8**, 3647-3654.
16. C. M. Hessel, D. Reid, M. G. Panthani, M. R. Rasch, B. W. Goodfellow, J. Wei, H. Fujii, V. Akhavan and B. A. Korgel, *Chem. Mater.*, 2012, **24**, 393-401.
17. L. M. Wheeler, N. R. Neale, T. Chen and U. R. Kortshagen, *Nature Commun.*, 2013, **4**, 2197.
18. Z. Ni, L. Ma, S. Du, Y. Xu, M. Yuan, H. Fang, Z. Wang, M. Xu, D. Li, J. Yang, W. Hu, X. Pi and D. Yang, *ACS Nano*, 2017, **11**, 9854-9862.
19. H. Sugimoto, R. Zhang, B. M. Reinhard, M. Fujii, G. Perotto, B. Marelli, F. G. Omenetto and L. Dal Negro, *Appl. Phys. Lett.*, 2015, **107**, 041111.
20. Y. Yu and B. A. Korgel, *Langmuir*, 2015, **31**, 6532-6537.
21. A. Marinins, Z. Yang, H. Chen, J. Linnros, J. G. C. Veinot, S. Popov and I. Sychugov, *ACS Photonics*, 2016, **3**, 1575-1580.
22. M. Dasog, J. Kehrle, B. Rieger and J. G. Veinot, *Angew Chem Int Ed Engl*, 2016, **55**, 2322-2339.
23. Y. Li, S. Yu, J. G. C. Veinot, J. Linnros, L. Berglund and I. Sychugov, *Advanced Optical Materials*, 2017, **5**, 1600834.
24. A. Marinins, R. Zandi Shafagh, W. van der Wijngaart, T. Haraldsson, J. Linnros, J. G. C. Veinot, S. Popov and I. Sychugov, *ACS Appl Mater Interfaces*, 2017, **9**, 30267-30272.
25. H. Sugimoto, Y. Ozaki and M. Fujii, *ACS Appl. Mater. Interfaces*, 2017, **9**, 19135-19142.
26. H. Sugimoto, T. Chen, R. Wang, M. Fujii, B. M. Reinhard and L. Dal Negro, *Acs Photonics*, 2015, **2**, 1298-1305.
27. A. Inoue, M. Fujii, H. Sugimoto and K. Imakita, *J. Phys. Chem. C*, 2015, **119**, 25108-25113.
28. A. Inoue, H. Sugimoto, H. Yaku and M. Fujii, *Rsc Advances*, 2016, **6**, 63933-63939.
29. S.-W. Lin and D.-H. Chen, *Small*, 2009, **5**, 72-76.
30. B. A. Manhat, A. L. Brown, L. A. Black, J. B. Ross, K. Fichter, T. Vu, E. Richman and A. M. Goforth, *Chemistry of materials : a publication of the American Chemical Society*, 2011, **23**, 2407-2418.
31. M. Fujii, H. Sugimoto and K. Imakita, *Nanotechnology*, 2016, **27**, 262001.
32. H. Sugimoto, M. Fujii and K. Imakita, *Nanoscale*, 2014, **6**, 12354-12359.

33. H. Sugimoto and M. Fujii, *Advanced Optical Materials*, 2017, **5**, 1700332.
34. T. Kanno, M. Fujii, H. Sugimoto and K. Imakita, *J. Mater. Chem. C*, 2014, **2**, 5644-5650.
35. H. Sugimoto, M. Fujii, K. Imakita, S. Hayashi and K. Akamatsu, *J. Phys. Chem. C*, 2013, **117**, 6807-6813.
36. M. Fukuda, M. Fujii, H. Sugimoto, K. Imakita and S. Hayashi, *Opt. Lett.*, 2011, **36**, 4026-4028.
37. H. Sugimoto, M. Fujii, K. Imakita, S. Hayashi and K. Akamatsu, *J. Phys. Chem. C*, 2012, **116**, 17969-17974.
38. H. Sugimoto, M. Fujii, Y. Fukuda, K. Imakita and K. Akamatsu, *Nanoscale*, 2014, **6**, 122-126.
39. L. Ostrovska, A. Broz, A. Fucikova, T. Belinova, H. Sugimoto, T. Kanno, M. Fujii, J. Valenta and M. H. Kalbacova, *Rsc Advances*, 2016, **6**, 63403-63413.
40. M. Fujii, H. Sugimoto, M. Hasegawa and K. Imakita, *J. Appl. Phys.*, 2014, **115**, 084301.
41. H. Sugimoto, M. Yamamura, M. Sakiyama and M. Fujii, *Nanoscale*, 2018, DOI: 10.1039/C7NR09474D.
42. H. Sugimoto, M. Fujii and K. Imakita, *Rsc Advances*, 2015, **5**, 8427-8431.
43. H. Sugimoto, K. Imakita and M. Fujii, *Rsc Advances*, 2015, **5**, 98248-98253.
44. O. C. Hellman, J. A. Vandenbroucke, J. Rüsing, D. Isheim and D. N. Seidman, *Microsc. Microanal.*, 2002, **6**, 437-444.
45. R. Khelifi, D. Mathiot, R. Gupta, D. Muller, M. Roussel and S. Duguay, *Appl. Phys. Lett.*, 2013, **102**, 013116.
46. H. Gnaser, S. Gutsch, M. Wahl, R. Schiller, M. Kopnarski, D. Hiller and M. Zacharias, *J. Appl. Phys.*, 2014, **115**, 034304.
47. K. Nomoto, H. Sugimoto, A. Breen, A. V. Cezguerra, T. Kanno, S. P. Ringer, I. P. Wurfl, G. Conibeer and M. Fujii, *J. Phys. Chem. C*, 2016, **120**, 17845-17852.
48. K. Nomoto, S. Gutsch, A. V. Ceguerra, A. Breen, H. Sugimoto, M. Fujii, I. Perez-Wurfl, S. P. Ringer and G. Conibeer, *MRS Communications*, 2016, **6**, 283-288.
49. T. Kanno, H. Sugimoto, A. Fucikova, J. Valenta and M. Fujii, *J. Appl. Phys.*, 2016, **120**, 164307.
50. M. D. Mason, G. M. Credo, K. D. Weston and S. K. Buratto, *Phys. Rev. Lett.*, 1998, **80**, 5405-5408.
51. J. Valenta, R. Juhasz and J. Linnros, *J. Lumin.*, 2002, **98**, 15-22.
52. D. S. English, L. E. Pell, Z. Yu, P. F. Barbara and B. A. Korgel, *Nano Lett.*, 2002, **2**, 681-685.
53. J. Martin, F. Cichos and C. von Borczyskowski, *J. Lumin.*, 2004, **108**, 347-350.
54. J. Valenta, A. Fucikova, F. Vácha, F. Adamec, J. Humpolíčková, M. Hof, I. Pelant, K. Kůsová, K. Dohnalová and J. Linnros, *Adv. Funct. Mater.*, 2008, **18**, 2666-2672.
55. J. Martin, F. Cichos, F. Huisken and C. von Borczyskowski, *Nano Lett.*, 2008, **8**, 656-660.
56. T. Schmidt, A. I. Chizhik, A. M. Chizhik, K. Potrick, A. J. Meixner and F. Huisken, *Phys. Rev. B*, 2012, **86**, 125302.
57. K. Kůsová, I. Pelant and J. Valenta, *Light: Science &Amp; Applications*, 2015, **4**, e336.
58. I. Sychugov, F. Pevere, J.-W. Luo, A. Zunger and J. Linnros, *Phys. Rev. B*, 2016, **93**, 161413.
59. I. Sychugov, A. Fucikova, F. Pevere, Z. Yang, J. G. C. Veinot and J. Linnros, *ACS Photonics*, 2014, **1**, 998-1005.
60. I. Sychugov, R. Juhasz, J. Valenta and J. Linnros, *Phys. Rev. Lett.*, 2005, **94**, 087405.
61. Y. Hori, S. Kano, H. Sugimoto, K. Imakita and M. Fujii, *Nano Lett.*, 2016, **16**, 2615-2620.
62. O. Ashkenazi, D. Azulay, I. Balberg, S. Kano, H. Sugimoto, M. Fujii and O. Millo, *Nanoscale*, 2017, **9**, 17884-17892.
63. O. Wolf, M. Dasog, Z. Yang, I. Balberg, J. G. C. Veinot and O. Millo, *Nano Lett.*, 2013, **13**, 2516-2521.
64. D. A. Kislitsyn, V. Kocevski, J. M. Mills, S. K. Chiu, C. F. Gervasi, B. N. Taber, A. E. Rosenfield, O. Eriksson, J. Rusz, A. M. Goforth and G. V. Nazin, *J Phys Chem Lett*, 2016, **7**, 1047-1054.
65. D. A. Kislitsyn, J. M. Mills, S. K. Chiu, B. N. Taber, J. D. Barnes, C. F. Gervasi, A. M. Goforth and G. V. Nazin, *J Phys Chem Lett*, 2018, **9**, 710-716.
66. I. Marri, E. Degoli and S. Ossicini, *Prog. Surf. Sci.*, 2017, **92**, 375-408.
67. R. Derian, K. Tokár, B. Somogyi, Á. Gali and I. Štich, *Journal of Chemical Theory and Computation*, 2017, **13**, 6061-6067.
68. D. Kovalev, E. Gross, N. Kunzner, F. Koch, V. Timoshenko and M. Fujii, *Phys. Rev. Lett.*, 2002, **89**.
69. E. Gross, D. Kovalev, N. Kunzner, J. Diener, F. Koch, V. Y. Timoshenko and M. Fujii, *Phys. Rev. B*, 2003, **68**, 115405.
70. M. Fujii, S. Minobe, M. Usui, S. Hayashi, E. Gross, J. Diener and D. Kovalev, *Phys. Rev. B*, 2004, **70**.
71. M. Fujii, M. Usui, S. Hayashi, E. Gross, D. Kovalev, N. Kunzner, J. Diener and V. Timoshenko, *J. Appl. Phys.*, 2004, **95**, 3689-3693.
72. D. Kovalev and M. Fujii, *Adv. Mater.*, 2005, **17**, 2531-2544.
73. M. Fujii, D. Kovalev, B. Goller, S. Minobe, S. Hayashi and V. Timoshenko, *Phys. Rev. B*, 2005, **72**, 165321.
74. N. J. Turro, *Modern Molecular Photochemistry*, University Science, Sau-salito, CA, 1991.
75. a. C. A. C. L. Gilbert, *Reactive Oxygen Species in Biological System* Plenum, New York, 1999.
76. L. P. a. H. Sies, *Singlet Oxygen, UV-A, and Ozone*, Academic, London, 2000.
77. J. G. Moser, *Photodynamic Tumor Therapy: 2nd and 3rd Generation Photosensitizers*, Harwood Academic Publishers, Amsterdam, 1998.
78. D. L. Dexter, *The Journal of Chemical Physics*, 1953, **21**, 836-850.
79. T. Kojima, H. Sugimoto and M. Fujii, *J. Phys. Chem. C*, 2018, **122**, 1874-1880.
80. A. B. Fischer and I. Bronstein-Bonte, *Journal of Photochemistry*, 1985, **30**, 475-485.
81. H. Sugimoto, Y. Hori, Y. Imura and M. Fujii, *J. Phys. Chem. C*, 2017, **121**, 11962-11967.
82. M. Fujii, M. Yoshida, Y. Kanzawa, S. Hayashi and K. Yamamoto, *Appl. Phys. Lett.*, 1997, **71**, 1198-1200.
83. M. Fujii, S. Hayashi and K. Yamamoto, *Appl. Phys. Lett.*, 1998, **73**, 3108-3110.
84. K. Watanabe, H. Tamaoka, M. Fujii and S. Hayashi, *J. Appl. Phys.*, 2002, **92**, 4001-4006.
85. A. J. Kenyon, *Semicond. Sci. Technol.*, 2005, **20**, R65-R84.
86. D. Timmerman, I. Izeddin, P. Stallinga, I. N. Yassievich and T. Gregorkiewicz, *Nature Photonics*, 2008, **2**, 105-109.
87. D. Timmerman, J. Valenta, K. Dohnalova, W. D. de Boer and T. Gregorkiewicz, *Nat Nanotechnol*, 2011, **6**, 710-713.
88. M. T. Trinh, R. Limpens, W. D. A. M. de Boer, J. M. Schins, L. D. A. Siebbeles and T. Gregorkiewicz, *Nat Photon*, 2012, **6**, 316-321.

89. Z. Lin, H. Li, A. Franceschetti and M. T. Lusk, *ACS Nano*, 2012, **6**, 4029-4038.
90. R. Limpens, A. Lesage, P. Stallinga, A. N. Poddubny, M. Fujii and T. Gregorkiewicz, *J. Phys. Chem. C*, 2015, **119**, 19565-19570.
91. G. Allan and C. Delerue, *Phys. Rev. B*, 2007, **75**, 195311.
92. K. Seino, F. Bechstedt and P. Kroll, *Phys. Rev. B*, 2012, **86**, 075312.
93. M. Govoni, I. Marri and S. Ossicini, *Nat Photon*, 2012, **6**, 672-679.
94. R. Guerra and S. Ossicini, *Phys. Rev. B*, 2013, **87**, 165441.
95. K. Furuta, M. Fujii, H. Sugimoto and K. Imakita, *J. Phys. Chem. Lett.*, 2015, **6**, 2761-2766.
96. M. Sasaki, S. Kano, H. Sugimoto, K. Imakita and M. Fujii, *J. Phys. Chem. C*, 2016, **120**, 195-200.
97. H. Sugimoto, K. Furuta and M. Fujii, *J. Phys. Chem. C*, 2016, **120**, 24469-24475.
98. T. Kanno, S. Kano, H. Sugimoto, Y. Tada and M. Fujii, *Mrs Communications*, 2016, **6**, 429-436.
99. R. Sinelnikov, M. Dasog, J. Beamish, A. Meldrum and J. G. C. Veinot, *ACS Photonics*, 2017, **4**, 1920-1929.
100. H. Sugimoto, M. Fujii and K. Imakita, *Nanoscale*, 2016, **8**, 10956-10962.
101. J. S. Biteen, D. Pacifici, N. S. Lewis and H. A. Atwater, *Nano Lett.*, 2005, **5**, 1768-1773.
102. J. S. Biteen, N. S. Lewis, H. A. Atwater, H. Mertens and A. Polman, *Appl. Phys. Lett.*, 2006, **88**, 131109.
103. R. J. Walters, J. Kalkman, A. Polman, H. A. Atwater and M. J. A. de Dood, *Phys. Rev. B*, 2006, **73**, 132302.
104. E. Takeda, T. Nakamura, M. Fujii, S. Miura and S. Hayashi, *Appl. Phys. Lett.*, 2006, **89**, 101907.
105. E. Takeda, M. Fujii, T. Nakamura, Y. Mochizuki and S. Hayashi, *J. Appl. Phys.*, 2007, **102**.
106. Y. Mochizuki, M. Fujii, S. Hayashi, T. Tsuruoka and K. Akamatsu, *J. Appl. Phys.*, 2009, **106**, 013517.
107. A. Inoue, H. Sugimoto and M. Fujii, *J. Phys. Chem. C*, 2017, **121**, 11609-11615.
108. H. Yanagawa, A. Inoue, H. Sugimoto, M. Shioi and M. Fujii, *J. Appl. Phys.*, 2017, **122**.
109. H. Sugimoto, S. Yashima, K. Furuta, A. Inoue and M. Fujii, *Appl. Phys. Lett.*, 2016, **108**.
110. S. Yashima, H. Sugimoto, H. Takashina and M. Fujii, *J. Phys. Chem. C*, 2016, **120**, 28795-28801.
111. R. Gresback, N. J. Kramer, Y. Ding, T. Chen, U. R. Kortshagen and T. Nozaki, *ACS Nano*, 2014, **8**, 5650-5656.
112. T. Chen, B. Skinner, W. Xie, B. I. Shklovskii and U. R. Kortshagen, *J. Phys. Chem. C*, 2014, **118**, 19580-19588.
113. T. Chen, K. V. Reich, N. J. Kramer, H. Fu, U. R. Kortshagen and B. I. Shklovskii, *Nat Mater*, 2015, **15**, 299-303.
114. W. Aigner, M. Wiesinger, H. Wiggers, M. Stutzmann and R. N. Pereira, *Physical Review Applied*, 2016, **5**, 054017.
115. K.-Y. Cheng, R. Anthony, U. R. Kortshagen and R. J. Holmes, *Nano Lett.*, 2010, **10**, 1154-1157.
116. K.-Y. Cheng, R. Anthony, U. R. Kortshagen and R. J. Holmes, *Nano Lett.*, 2011, **11**, 1952-1956.
117. F. Maier-Flaig, J. Rinck, M. Stephan, T. Bocksrocker, M. Bruns, C. Kubel, A. K. Powell, G. A. Ozin and U. Lemmer, *Nano Lett.*, 2013, **13**, 475-480.
118. L. Yao, T. Yu, L. Ba, H. Meng, X. Fang, Y. Wang, L. Li, X. Rong, S. Wang, X. Wang, G. Ran, X. Pi and G. Qin, *J. Mater. Chem. C*, 2016, **4**, 673-677.
119. C.-Y. Liu, Z. C. Holman and U. R. Kortshagen, *Nano Lett.*, 2008, **9**, 449-452.
120. Y. Ohata, H. Sugimoto and M. Fujii, *Nanoscale*, 2018, DOI: 10.1039/C8NR00631H.
121. S. Kano, M. Sasaki and M. Fujii, *J. Appl. Phys.*, 2016, **119**.
122. S. Kano, K. Kim and M. Fujii, *Acs Sensors*, 2017, **2**, 828-833.
123. S. Kano, Y. Dobashi and M. Fujii, *IEEE Sensors Letters*, 2018, **2**, 1-4.
124. Y. Higashikawa, Y. Azuma, Y. Majima, S. Kano and M. Fujii, *Appl. Phys. Lett.*, 2016, **109**.
125. A. Mazurak, R. Mroczynski, J. Jasinski, D. Tanous, B. Majkusiak, S. Kano, H. Sugimoto, M. Fujii and J. Valenta, *Microelectron. Eng.*, 2017, **178**, 298-303.
126. T. Belinova, L. Vrabcova, I. Machova, A. Fucikova, J. Valenta, H. Sugimoto, M. Fujii and M. H. Kalbacova, *Physica status solidi (b)*, 2018, DOI: 10.1002/pssb.201700597.
127. A. M. Smith, M. C. Mancini and S. Nie, *Nature Nanotech.*, 2009, **4**, 710-711.
128. J. Joo, X. Liu, V. R. Kotamraju, E. Ruoslahti, Y. Nam and M. J. Sailor, *ACS Nano*, 2015, **9**, 6233-6241.
129. L. Gu, D. J. Hall, Z. Qin, E. Anglin, J. Joo, D. J. Mooney, S. B. Howell and M. J. Sailor, *Nature Commun.*, 2013, **4**, 2326.
130. A. I. Kuznetsov, A. E. Miroshnichenko, M. L. Brongersma, Y. S. Kivshar and B. Luk'yanchuk, *Science*, 2016, **354**.
131. H. Sugimoto and M. Fujii, *ACS Photonics*, 2018, DOI: 10.1021/acsphotonics.7b01461.